

Impact of free electron laser coherence on imaging quality

Shuang Wei(魏爽), Shuang Gong(龚爽), Yang Bu(步扬), and Zi-Jian Song(宋子健)
Citation: Chin. Phys. B, 2025, 34 (**5**): 054201. DOI: 10.1088/1674-1056/adb734
http://cpb.iphy.ac.cn; http://iopscience.iop.org/cpb

What follows is a list of articles you may be interested in

Nonclassicality of photons in mean-field anisotropic quantum light-matter interacting lattices: Two-photon correlation function and quadrature squeezing

Xu-Min Chen(陈许敏), Pei-Yao Chen(陈佩瑶), and Chen Wang(王晨)
Chin. Phys. B, 2025, 34 (**4**): 044201. DOI: 10.1088/1674-1056/ada9db

Optical design of the time-resolved ARPES beamline of the new material spectroscopy experimental station for the update of CAEP THz-FEL facility

Liang-Liang Du(杜亮亮), Li-Min Meng(孟立民), Jiang Li(李江), and Li-Guo Zhu(朱礼国)
Chin. Phys. B, 2024, 33 (**11**): 114203. DOI: 10.1088/1674-1056/ad73b1

Robust autofocusing propagation in turbulence

Na-Na Liu(刘娜娜), Liu Tan(谭柳), Kai-Jian Chen(陈凯健), Pei-Long Hong(洪佩龙), Xiao-Ming Mo(莫小明), Bing-Suo Zou(邹炳锁), Yu-Xuan Ren(任煜轩), and Yi Liang(梁毅)
Chin. Phys. B, 2024, 33 (**6**): 064201. DOI: 10.1088/1674-1056/ad2bf4

A polarization sensitive interferometer: Delta interferometer

Chao-Qi Wei(卫超奇), Jian-Bin Liu(刘建彬), Yi-Fei Dong(董翼飞), Yu-Nong Sun(孙雨农), Yu Zhou(周宇), Huai-Bin Zheng(郑淮斌), Yan-Yan Liu(刘严严), Xiu-Sheng Yan(闫秀生), Fu-Li Li(李福利), and Zhuo Xu(徐卓)
Chin. Phys. B, 2024, 33 (**3**): 034203. DOI: 10.1088/1674-1056/acf996

Spatial quantum coherent modulation with perfect hybrid vector vortex beam based on atomic medium

Yan Ma(马燕), Xin Yang(杨欣), Hong Chang(常虹), Xin-Qi Yang(杨鑫琪), Ming-Tao Cao(曹明涛), Xiao-Fei Zhang(张晓斐), Hong Gao(高宏), Rui-Fang Dong(董瑞芳), and Shou-Gang Zhang(张首刚)
Chin. Phys. B, 2024, 33 (**2**): 024204. DOI: 10.1088/1674-1056/ad0f86

Impact of free electron laser coherence on imaging quality

Shuang Wei(魏爽)[1], Shuang Gong(龚爽)[2,†], Yang Bu(步扬)[3,‡], and Zi-Jian Song(宋子健)[1]

[1] *School of Microelectronics, Shanghai University, Shanghai* 200444, *China*
[2] *Zhangjiang Laboratory, Shanghai* 201210, *China*
[3] *Shanghai Institute of Optics and Fine Mechanics, Chinese Academy of Sciences, Shanghai* 201800, *China*

(Received 1 December 2024; revised manuscript received 7 February 2025; accepted manuscript online 18 February 2025)

The high temporal and spatial coherence of free electron lasers (FELs) reduces the uniformity of the illumination field, leading to scattering effects that blur the edges of patterns, resulting in diminished accuracy and clarity. Traditional imaging models regard the light source as fully incoherent, making it difficult to assess the impact of partially coherent light fields on imaging. If FELs are used in imaging systems, their coherence must be considered. To address this issue, this study explores the relationship between coherence, imaging quality and speckle contrast through a simulation method based on random phases. The method divides the light beam into temporal and spatial coherence cells, analyzes their interactions, and simulates imaging results under different coherence conditions. Additionally, speckle patterns for various illumination modes are calculated to evaluate their effects on speckle contrast and illumination uniformity. The results indicate that under different illumination modes, illumination uniformity decreases as coherence increases, while speckle contrast increases with higher coherence. In terms of imaging quality, higher coherence leads to an increase in both line edge roughness (LER) and line width roughness (LWR), thereby reducing the imaging quality. Additionally, the narrower the line width, the greater the impact of coherence on the imaging quality, resulting in poorer imaging performance.

Keywords: free electron laser, coherence, imaging, speckle contrast, field uniformity

PACS: 42.25.Kb, 42.30.–d, 42.55.–f, 41.60.Cr

DOI: 10.1088/1674-1056/adb734 **CSTR:** 32038.14.CPB.adb734

1. Introduction

Free electron lasers (FELs) have the characteristics of high coherence and high collimation, enabling them to produce highly powerful beams with precisely controlled wavelengths.[1] The FEL relies on the principle of synchrotron radiation, which states that when a high-energy, relativistic charged particle undergoes radial acceleration, photons are emitted to satisfy the physical principle of energy conservation. Its radiation wavelength is continuously tunable, and its high-power femtosecond pulses have broad application potential.

A FEL generates laser radiation through free electrons in a vacuum, with core components including the electron source and the magnetic undulator.[2] Electrons become polarized in a magnetic field, following a sinusoidal trajectory. Electrons produce electromagnetic radiation (light pulses) as they perform undulating motion. The light pulses are reflected by upstream and downstream mirrors, repeatedly interacting with subsequent electron bunches. As a result, the electrons cluster along the direction of motion into micro-bunches smaller than the wavelength of the light. These micro-bunches convert their kinetic energy into the energy of the optical field, increasing the amplitude of the light field. This process repeats multiple times until the light intensity reaches saturation. The electrons, after their interaction, are deflected out of the system by downstream bending magnets.

The concept of the FEL was first proposed by Madey in 1971.[3] Since then, at least 50 FEL facilities have been established worldwide. Notable facilities include the JLab FEL in the United States of America,[4,5] the Novosibirsk FEL in Russia,[6] the ALICE FEL in the United Kingdom,[7] and the JAEA FEL in Japan. As early as around the year 2000, the China Academy of Engineering Physics conducted theoretical and simulation research on energy recovery linear accelerators and proposed a design plan for a kW-level FEL based on an ERL device.[8] Building on years of research in radiofrequency superconducting accelerators, Peking University proposed the design plan for the Peking University ERL FEL[9] and carried out research work on ERL beam dynamics design[10] and analysis of beam breakup (BBU) effects.[11]

At the beginning of the 21st century, a proposal to use FELs as high-power next-generation light sources was presented.[12,13] FEL technology offers several advantages, including the absence of fragment and particle contamination, no requirement for large aperture collector mirrors, low thermal deposition, high average power, and beam quality near the diffraction limit.[14,15] In addition, in terms of imaging, compared to conventional lasers, FELs can offer tunable wavelengths ranging from ultraviolet to x-rays. The tunability

†Corresponding author. E-mail: gongshuang@zjlab.ac.cn
‡Corresponding author. E-mail: buyang@siom.ac.cn

© 2025 Chinese Physical Society and IOP Publishing Ltd. All rights, including for text and data mining, AI training, and similar technologies, are reserved.

of the FELs allows for the selection of the optimal wavelength for different imaging applications, thereby achieving higher resolution. The FEL has a smaller divergence angle, enabling higher-resolution images. Despite these many advantages, FELs face challenges due to their highly coherent light sources, which are prone to producing speckle noise. Coherence-induced speckle effects result in a reduced process window. Additionally, the high spatial frequency nonuniformity in the light field caused by the coherence of the light source is difficult to correct using current uniformity correction techniques, such as gray filter plates or microlens arrays.[16]

In recent years, researchers have also proposed many methods to reduce the effects caused by the high coherence of FELs. For example, based on Fourier synthesis theory, the Lawrence Berkeley National Laboratory uses a Fourier synthesis illuminator to reduce spatial coherence. This method has been proven to provide nearly fully spatially coherent illumination. However, the coherence control time achieved by this system is relatively long.[17] It is often desirable to control the illumination shape, uniformity, and spatial coherence in imaging systems. Holographic optical elements (HOEs) provide a means to do this by enabling custom far-field patterns to be generated from a coherent source. The Anderson *et al*. team proposed a method to mitigate speckle using time-varying pure phase HOEs and a scanning subsystem. This system can homogenize and shape high-coherence light sources into any form in systems with integration times exceeding 100 ms, with a speckle contrast of less than 1%.[18] This study demonstrates that reducing the coherence of the light source can make the light source more uniform, decrease the speckle contrast, and ultimately improve the imaging quality. Naulleau *et al.*'s team upgraded the Berkeley 0.3-NA micro-field exposure tool and redesigned the programmable coherent illumination system to provide better field uniformity.[19] The research methods listed above have effectively mitigated the impact of the FEL's high coherence on imaging quality. Understanding how the high coherence of FELs affects the quality of imaging patterns requires an interpretation through relevant technical metrics. However, traditional imaging models typically regard the light source as fully incoherent, making it challenging to provide a proper explanation. Therefore, a new partially coherent imaging model is urgently needed. This paper proposes a partially coherent illumination simulation method based on mutual intensity propagation theory, analyzing the imaging results under light sources with different coherence levels and evaluating the corresponding image quality metrics.

2. Working principle

2.1. Coherence theory

Coherence is one of the key properties of a light field, and is divided into temporal coherence and spatial coherence.[20] Temporal coherence refers to the correlation of the light field at different moments at the same spatial point, while spatial coherence refers to the correlation of the light field at different spatial points at the same time. In 1802, Young observed alternating bright and dark fringes in his double-slit interference experiment,[21] which opened the door to the study of optical coherence. Figure 1 shows a schematic diagram of Young's interference experiment.[22,23] The light intensity distribution on the observation screen in Fig. 1 is as follows:

$$I = I_1 + I_2 + 2\sqrt{I_1 I_2}\,|\gamma_{12}|\cos\left[\arg\left(\gamma_{12}\right)\right], \tag{1}$$

with I_1 and I_2 representing the light intensities passing through apertures S_1 and S_2, respectively, and γ_{12} representing the complex coherence of the light field. The visibility of the interference fringes is defined as

$$K = \left(I_{\max} - I_{\min}\right) / \left(I_{\max} + I_{\min}\right). \tag{2}$$

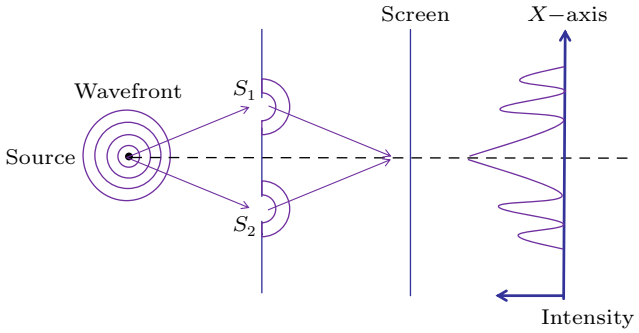


Fig. 1. Young's interferometry.

For a partially coherent light field $U(x,t)$, the light oscillations exhibit random fluctuations in both space and time. Such random disturbances in a partially coherent light field at different times or spatial locations cannot be fully described by a two-dimensional complex amplitude function $U(x)$ alone. Instead, statistical methods are required to describe the coherence of the light field.

For a stationary, ergodic light wave field, the spatiotemporal coherence of the light beam can be represented by the mutual coherence function $\Gamma(x_1,x_2,\tau)$,[24] which is defined as follows:

$$\begin{aligned}\Gamma\left(x_1,x_2,\tau\right) &= \left\langle U\left(x_1,t_1\right)U^*\left(x_2,t_2\right)\right\rangle \\ &= \left\langle U\left(x_1,t\right)U^*\left(x_2,t+\tau\right)\right\rangle,\end{aligned} \tag{3}$$

where $\tau = t_2 - t_1$, and the angle brackets denote taking the time average. The complex degree of coherence is defined as the normalized function of the mutual coherence function[25,26]

$$\gamma(x_1,x_2,\tau) = \frac{\Gamma\left(x_1,x_2,\tau\right)}{\sqrt{\Gamma\left(x_1,x_1,0\right)\Gamma\left(x_2,x_2,0\right)}}$$

$$= \frac{\Gamma(x_1, x_2, \tau)}{\sqrt{I_1(x_1) I_2(x_2)}}. \tag{4}$$

The two types of coherence in a light field — temporal and spatial — can be described using the mutual coherence function. By focusing only on the effect of time delay and ignoring spatial differences, the autocorrelation function represents temporal coherence. Spatial coherence is typically analyzed under the 'quasi-monochromatic' condition and a small optical path difference, allowing the light field's coherence to approximate spatial coherence. Therefore, the physical quantity $\Gamma(x_1, x_2, 0)$, which characterizes spatial coherence under quasi-monochromatic conditions, is defined as the mutual intensity $J(x_1, x_2)$:

$$J(x_1, x_2) = \Gamma(x_1, x_2, 0) = \langle U(x_1, t) U^*(x_2, t) \rangle. \tag{5}$$

Incoherent imaging and coherent imaging represent two extreme and ideal cases. The one more commonly encountered is partially coherent imaging. When partially coherent light is used for imaging, the system behaves as a linear system with respect to the mutual intensity of light. It can be represented by a quadruple overlap integral:

$$\tilde{J}(\xi_1, \eta_1; \xi_2, \eta_2) = \int_{+\infty}^{-\infty} \int_{+\infty}^{-\infty} \tilde{J}(x_1, y_1; x_2, y_2) \tilde{K}(\xi_1, \eta_1; x_1, y_1) \times \tilde{K}^*(\xi_2, \eta_2; x_2, y_2) \, \mathrm{d}x_1 \, \mathrm{d}y_1 \, \mathrm{d}x_2 \, \mathrm{d}y_2. \tag{6}$$

The $\tilde{K} \cdot \tilde{K}^*$ corresponds to the impulse response of the system, which can also be referred to as the system's scattering function. This equation expresses the propagation relationship between the mutual intensity $J(x_1, x_2, y_1, y_2)$ between two points on plane Σ_1 and the mutual intensity $J(\xi_1, \eta_1, \xi_2, \eta_2)$ between two points on plane Σ_2. The above equation indicates that the propagation of mutual intensity can be regarded as a linear system. According to Goodman's theory of Fourier optics, in the case of partially coherent light imaging, the system behaves as a linear system with respect to the mutual intensity of light.[27] Based on linear system theory, the mutual intensity on the Σ_2 plane can be obtained by linearly superimposing all responses with $J(x_1, x_2, y_1, y_2)$ as the weighting factor.

2.2. Partial coherence illumination based on mutual intensity propagation theory

To understand the relationship between spatial and temporal coherence and the contrast of speckle patterns, a simplified partial coherence illumination model has been established based on the mutual intensity propagation theory and building upon Noordman's research.[28] Research shows that the contrast of the speckle pattern is caused by the combined effects of the temporal and spatial coherence of light. The temporal component is determined by the bandwidth of the laser source and the duration of the laser pulse, while the spatial distribution of the speckle pattern depends on the intensity distribution of light in the pupil. As shown in Fig. 2, a linearly polarized laser beam, with spatial coherence area A_c and temporal coherence function τ_c , illuminates the mask surface.

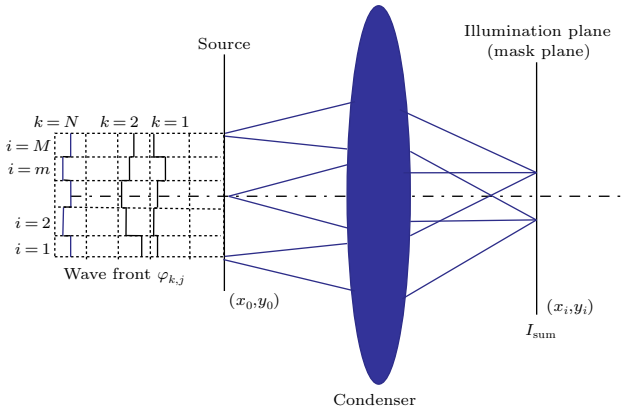


Fig. 2. Partial coherence illumination based on mutual intensity propagation theory. A microlens array is placed at the point where the light beam enters, dividing the beam into sub-beams. These sub-beams are then reflected by micro-mirrors onto the condenser lens, which focuses them onto the illumination pupil plane. By adjusting the angle of the micro-mirrors, the position of the sub-beams on the pupil plane can be altered, allowing for multiple illumination modes.

A slightly simplified method was used, dividing the light field into N temporal coherence cells and M micro-reflector spatial cells. It is assumed that the light field space within the micro-reflector space is fully coherent. According to the definition of spatial coherence, the light within a coherence cell has a temporally stable wavefront. However, due to the temporal coherence of light, the phase will still undergo random fluctuations over time,[29] but these changes are the same for the entire spatial coherence cell. Therefore, we define $N \times M$ random phases $\varphi_{k,i}$ for all combinations of temporal coherence cell k and spatial coherence cell i.

When the light from a single spatial coherence cell i generates a fixed electromagnetic field on the observation plane, it is described by E_i whose intensity distribution is $J_i = (E_i \cdot E_i^*)$. It is important to recognize that any instantaneous combination of electromagnetic fields must be summed based on the complex amplitude rather than intensity, regardless of spatial coherence (coherence manifests in time accumulation). Therefore, for a temporal coherence cell k, the electric fields E_i from M different spatial coherence cells must be summed on the complex amplitude basis considering the phase $\varphi_{k,i}$. The electric field intensity pattern on the observation plane is $I_k = (F_k \cdot F_k^*)$. Here, it is assumed that the time delay caused by the path length differences at the observation plane is negligible compared to the temporal coherence. First, assume that all components of the system are ideally manufactured without high-frequency phase modulation. The light field formed by the spatial coherence cells on the mask surface is an ideal

plane wave inclined at a certain angle. The instantaneous intensity distribution of the illumination light field is shown in Fig. 3. The speckle structure differences produced by different illumination modes are significant, and the contrast of each speckle pattern is 1. The speckle structure and scale depend on the wavelength, numerical aperture, and illumination mode, referring to the instantaneous intensity distribution of the illumination light field.

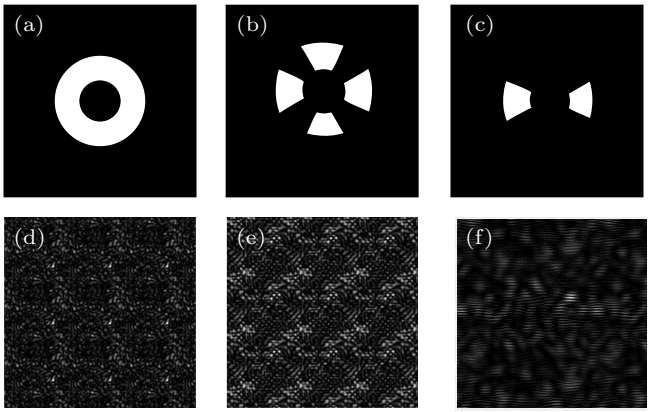


Fig. 3. Speckle patterns under different illumination pupil modes. (a) Annular mode; (b) cross quadrupole mode; (c) dipole mode; (d)–(f) corresponding speckle patterns.

For a temporal coherence cell k, the complex amplitude E_i from M different spatial coherence cells must be summed, taking into account the phase $\varphi_{k,i}$, resulting in the cumulative complex amplitude F_k:

$$F_k = \sum_{i=1}^{M} E_i \cdot \exp\left(\mathrm{i}\varphi_{k,i}\right). \tag{7}$$

The light field intensities from consecutive N temporal coherence cells are summed, resulting in an accumulated intensity on the observation plane, normalized as

$$I_{\text{sum}} = \frac{1}{N}\sum_{k=1}^{N} I_k = \frac{1}{N}\sum_{k=1}^{N} F_k \cdot F_k^*. \tag{8}$$

Normalize the intensity I_{sum}, when $i = j$, $\overline{E_i \cdot E_j^*} = 1$, when $i \neq j$, $\overline{E_i \cdot E_j^*} = 0$.

$$\begin{aligned} I_{\text{sum}} &= \frac{1}{M}\cdot\sum_{i=1}^{M} E_i \cdot E_i^* \\ &+ \frac{1}{N\cdot M}\sum_{k=1}^{N}\sum_{i=1}^{M}\sum_{j=1,j\neq i}^{M} E_i \cdot E_j^* \cdot \exp\left[\mathrm{i}\left(\varphi_{k,i}-\varphi_{k,j}\right)\right]. \end{aligned} \tag{9}$$

The two terms before and after summation can be regarded as the direct current (DC) term I_{DC} and the alternating current (AC) term I_{AC}.

$$I_{\text{sum}} = I_{\text{DC}} + I_{\text{AC}}. \tag{10}$$

Here, the first term is the DC component, which is the sum of the intensities of the light fields produced by the M spatial coherence cells. Because no additional phase modulation is introduced, the light intensity is completely uniform, and the speckle contrast is 0.

The second term is the AC component, which describes the interference cross-term between the field E_i and the field E_j^*, arriving at the observation plane within the same temporal coherence interval. This term has an average value of zero but introduces intensity modulation. Since E_i only depends on the spatial variable, the summation order can be exchanged, and the AC term can be written as

$$I_{\text{AC}} = \sum_{i=1}^{M}\sum_{j=1,j\neq i}^{M} E_i \cdot E_j^* \frac{1}{N}\sum_{k=1}^{N}\exp\left[\mathrm{i}\left(\varphi_{k,i}-\varphi_{k,j}\right)\right], \tag{11}$$

$$J_{ij,N} = \left|\frac{1}{N}\sum_{k=1}^{N}\exp\left[\mathrm{i}\left(\varphi_{k,i}-\varphi_{k,j}\right)\right]\right|. \tag{12}$$

Let $J_{ij,N}$ represent the correlation of the light field fluctuations between regions i and j over N temporal coherence cells. This can be understood as the statistical correlation of the light fields over a finite integration time. In the case where N is infinite, the above expression transforms into an integral form; $J_{ij,N}$ approaches the strictly defined spatial coherence (complex degree of spatial coherence):

$$\begin{aligned} J_{ij,\infty} &= \left|\lim_{N\to\infty}\frac{1}{N}\sum_{k=1}^{N}\exp\left[\mathrm{i}\left(\varphi_{k,i}-\varphi_{k,j}\right)\right]\right| \\ &\to \left|\lim_{T\to\infty}\int_0^T \exp\left[\mathrm{i}\left(\varphi(k,i)-\varphi(k,j)\right)\right]\mathrm{d}t\right|, \end{aligned} \tag{13}$$

where T represents the integration time. By introducing $J_{ij,N}$, the above spatiotemporal problem is simplified into a spatial variable problem, with the temporal factors (the number of temporal cell N and the light field disturbances over time) being uniformly expressed by $J_{ij,N}$. For example, when the integration time includes only one temporal coherence cell ($N = 1$), the random phase difference within the spatial coherence cell is fixed (even if the integration time is long), and all spatial coherence cells are mutually fully coherent. The accumulated intensity distribution is then the same as the instantaneous intensity, with a speckle contrast of 1.

The normalized intensity is written as

$$I_{\text{sum}} = \sum_{i=1}^{M} E_i \cdot E_i^* + \sum_{i=1}^{M}\sum_{j=1,j\neq i}^{M} E_i \cdot E_j^* \cdot J_{ij,N}. \tag{14}$$

Since $J_{ij,N} = 1$, $i = j$:

$$I_{\text{sum}} = \sum_{i=1}^{M}\sum_{j=1}^{M} E_i \cdot E_j^* \cdot J_{ij,N}. \tag{15}$$

The above formula is equivalent to the mutual intensity transmission formula of the light field, assuming that the total energy of the light field formed by each micro-reflector is the

same. The speckle or uniformity of the illumination light field completely depends on the spatial coherence of the light field within the finite time integration of the micro-reflectors.

2.3. Coherent and partially coherent imaging

Photolithography projects a mask image onto a photoresist-coated silicon wafer through a lens.[29] The optical system of modern photolithography machines consists of an illumination system and an imaging system. The illumination system adjusts the light source to achieve various partial coherence states, meeting exposure needs for different pattern shapes and densities. The optical model is based on Hopkins' optical imaging theory, which pre-calculates the transmission cross-coefficients (TCCs) to describe optical imaging. In the optical model, the optimized light source is directed through the illumination system onto the mask. If, in actual production, the wavelength of the incident light is larger than the mask line width, the imaging effect is dominated by diffraction. Some diffraction orders pass through the projection system's numerical aperture (NA) to the incident light pupil, and then imaging occurs. The mask image obtained earlier, after being processed by the optical model, results in the spatial image of the mask pattern, as shown in Fig. 4, where parallel incident light reaches the mask at maximum oblique angles. This method ensures that each point on the mask receives parallel light from different angles.[30–32] This prevents illumination system defects, especially from the diffuser, from being projected onto the mask, thus avoiding imaging defects.

The light emitted by an ideal monochromatic point source is fully coherent. However, real physical light sources are not point sources; they always have a certain spatial extent and consist of many radiating elements. The light they emit is not strictly monochromatic, as its spectrum has a certain width. This type of light is known as partially coherent light.

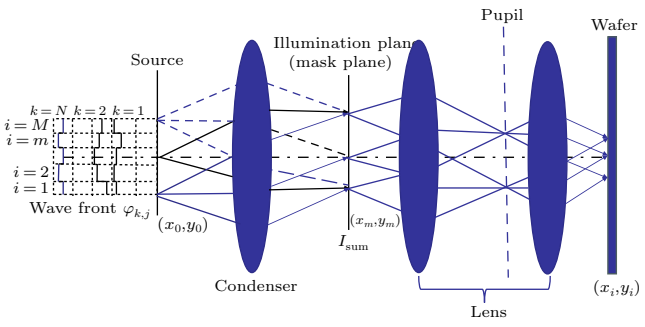


Fig. 4. Schematic diagram of a Kohler illumination system. The light source is divided into several sub-beams by the device, which are then projected onto the mask after passing through a lens. These sub-beams are subsequently combined by an imaging system composed of a lens group and pupil, and finally superimposed onto the image plane.

Assuming the coordinates of a certain light source point on the source plane are (x_0, y_0), the coordinates on the mask plane are (x_m, y_m), and the coordinates in the phase plane are (x_i, y_i), we can obtain

$$\begin{aligned} U_i(x_i,y_i) &= U_i\left(\frac{x_m}{M},\frac{y_m}{M}\right) \\ &= \mathcal{F}^{-1}\left\{U_m\left(x_m-x_f,y_m-y_f\right)\cdot \text{pupil}\right\}, \end{aligned} \tag{16}$$

where U_m and U_i represent the complex amplitude distributions of the object and image, respectively, pupil is the system's aperture function, x_f, y_f represent the spatial displacement caused by the off-axis illumination, and M is the magnification of the illumination system. $\mathcal{F}^{-1}$ represents the inverse Fourier transform. Traditional imaging only considers the case of normal incident light on the mask. Due to this fact, in this paper, we consider oblique incidence and the presence of a random phase. Therefore, the final complex amplitude distribution in the image plane, $E_{\text{image}}(x_i, y_i)$, is given by

$$\begin{aligned} E_{\text{image}}(x_i,y_i) &= U_i(x_i,y_i) \\ &\times \exp\left\{\mathrm{i}k\left[x_m\sin\left(\theta_{x_m}\right)+y_m\sin\left(\theta_{y_m}\right)\right]+\mathrm{i}\varphi_{\text{r}}\right\}, \end{aligned} \tag{17}$$

where θ_{x_m} and θ_{y_m} represent the angles of inclination in the x and y directions, respectively, and φ_{r} represents the random phase.

$$\begin{aligned} I_{\text{sum}} &= \sum_{i=1}^{M} E_i(x_i,y_i)\cdot E_i^*(x_i,y_i) \\ &+\sum_{i=1}^{M}\sum_{j=1,j\neq i}^{M} E_i(x_i,y_i)\cdot E_j^*(x_j,y_j)\cdot J_{ij,N}. \end{aligned} \tag{18}$$

2.4. Speckle contrast

We study the relationship between coherence and speckle contrast. Speckle contrast is defined as the ratio of the standard deviation of light intensity to the mean light intensity, expressed as

$$C = \frac{\sigma}{\overline{I_{\text{sum}}}}. \tag{19}$$

Here, σ represents the standard deviation of light intensity. Based on the relationship between the variance, standard deviation and mean, equation (19) can be rewritten as

$$C = \frac{\sqrt{\overline{I_{\text{sum}}^2}-\overline{I_{\text{sum}}}^2}}{\overline{I_{\text{sum}}}}. \tag{20}$$

Assuming that all spatial units are independent of each other and the light intensities are equal, we can obtain

$$C = \frac{\sqrt{M\cdot(M-1)\cdot\sum_{i=1}^{M}\sum_{j=1,j\neq i}^{M} J_{ij,N}\cdot J_{ji,N}}}{M}. \tag{21}$$

Set the distance between two points as ρ_{ij}. In the case of complete coherence, $J = 1$; in the case of complete incoherence, $J = \delta(\rho_{ij})$. For all other points, except for the points themselves, the coherence is 0. In the case of partial coherence, $J = F(\rho_{ij})$. Assuming the diameter of the light source is D,

the distance at the i spatial coherence unit is $l_i = \frac{D}{N} \cdot i$. Thus, we can obtain

$$C = \frac{\sqrt{M \cdot (M-1) \cdot \sum_{i=1}^{M} \sum_{j=1, j\neq i}^{M} F^2 \left(D/N \cdot |i-j|\right)}}{M}. \quad (22)$$

From Eq. (22), it can be seen that the speckle contrast C is highly dependent on the number of spatial coherence cells M and the distance between the two points.

3. Results and discussion

3.1. The number of temporal cells N affects J

According to the expression

$$J_{ij,N} = \left| \frac{1}{N} \sum_{k=1}^{N} \exp\left[\mathrm{i}\left(\varphi_{k,i} - \varphi_{k,j}\right)\right] \right|,$$

this depends on the range of phase fluctuations between the two spatial cells over time and the number of temporal coherence cells N within the integration time. As previously discussed, when $N = 1$, $J = 1$, completely independent of the temporal phase fluctuations. There are two scenarios where $N = 1$: (i) When the spectrum is ideal monochromatic light with a bandwidth of 0, the temporal coherence length is infinite, and N is 1 for any integration time. This indicates that when the beam is fully temporally coherent, it also possesses perfect spatial coherence. (ii) When the beam has a certain bandwidth, and the integration time is very short, including only one temporal coherence cell, N is 1. This is equivalent to capturing the instantaneous light intensity over an extremely short integration time, and the result does not reflect the cumulative effect of the light field fluctuations over time. These two cases have entirely different physical meanings.

When N approaches infinity or is sufficiently large, J can be equivalent to the traditionally defined spatial coherence of the light field, only affected by the temporal phase fluctuations, converging to the spatial coherence of the two points and not changing over time. When N is much greater than 1 but not enough to make $J_{ij,N}$ converge, which is the most common situation, J varies with time. Assuming the two spatial cells are completely incoherent, $\varphi_{k,i}$ and $\varphi_{k,j}$ are completely independent. According to the definition of coherence, under infinitely long-time integration, $J = 0$. We independently calculate 10000 integration time intervals and analyze the fluctuation of J for different values of N, as shown in Figs. 5 and 6.

The expected value and standard deviation are as follows. Even if the light fields at two spatial points fluctuate completely independently, residual coherence will still exist within a finite integration time. When the number of temporal coherence cells N within the integration time is small, J will fluctuate widely, manifesting as large fluctuations in speckle contrast over time. As N increases, the fluctuations of J decrease, and its standard deviation gradually converges to 0. Since the light field fluctuations are completely independent, the mean of J also decreases to 0. If the light fields at the

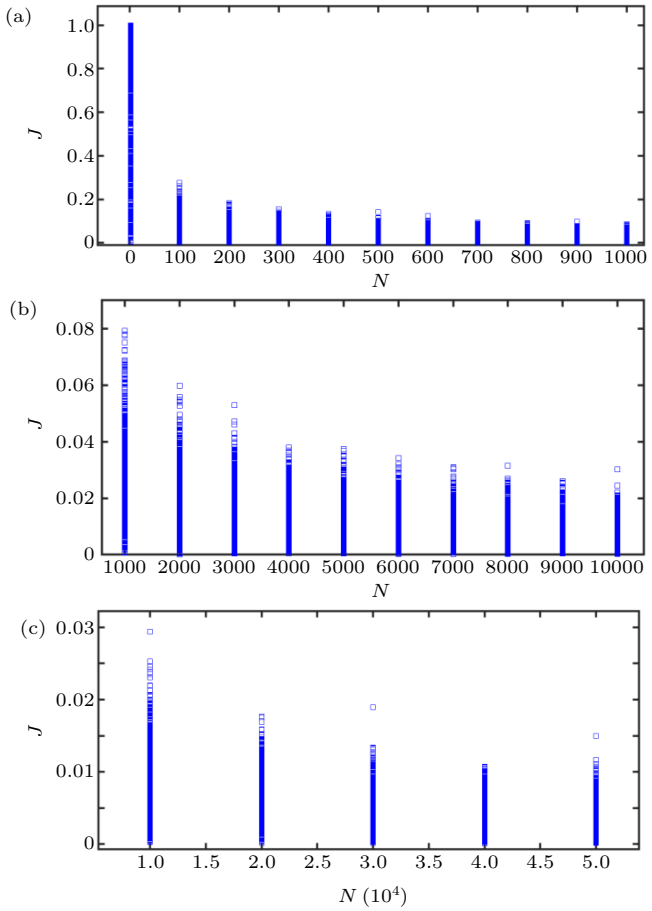


Fig. 5. The influence of time coherent cells on J (N = 1–50000).

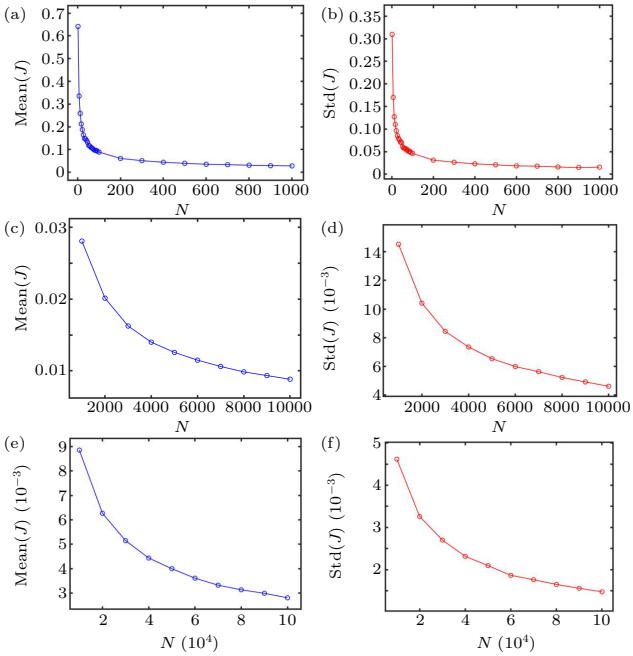


Fig. 6. Expectation and standard deviation of spatial coherence N = (1–50000).

spatial points inherently possess some spatial coherence, the mean will converge to that value.

The J can be characterized and detected by the fringe contrast of interference experiments within a specific integration time. Supposing the lithography illumination consists of only two discrete light source points, the illumination light field on the mask will show interference fringes. The contrast of these fringes represents the J of these two spatial points within a certain integration time. As the number of light source points increases, the interference fringes transform into speckles.

In the subsequent analysis and discussion, we will only analyze the impact of J on the lithography performance. The factors previously discussed, such as integration time and temporal coherence length, are already included.

3.2. The number of light source points k and J

First, consider two extreme cases. Under completely incoherent conditions, $J = 0$ and the cross term are entirely eliminated, resulting in $I_{\text{sum}} = \sum_{i=1}^{M} E_i \cdot E_i^*$, indicating complete incoherence between any two coherence cells. The illumination light field is the intensity superposition of the light fields formed by each coherence cell, yielding a completely uniform illumination light field with a speckle contrast of 0. In this and the following simulation calculations discussed, the NA is set to 0.33.

In the case of complete coherence, $J_{ij,N} = 1$:

$$I_{\text{sum}} = \sum_{i=1}^{M}\sum_{j=1}^{M} E_i \cdot E_j^* = \sum_{i=1}^{M} E_i \cdot \sum_{i=1}^{M} E_i^*, \tag{23}$$

indicating complete coherence between any two coherence cells. The illumination light field is the complex amplitude superposition of the light fields formed by each coherence cell, resulting in a fixed speckle pattern that does not change over time. The accumulated intensity distribution is the same as the instantaneous intensity distribution, with an illumination light field uniformity of 0% and a speckle contrast of 1.

Complete coherence and incoherence are theoretical extremes, while practical coherence is typically partial. Due to limited integration time and residual coherence between micro-reflectors, the mutual intensity superposition of coherence cells results in speckle contrast values between 0 and 1. Assuming equal coherence between any two cells and a light source with 200 points, we simulated speckle patterns under different coherence levels for ring and secondary illumination, calculating speckle contrast and light field uniformity. The speckle contrast is defined as the standard deviation of intensity divided by the mean intensity.

We simulated mask field imaging using dipole and annular illumination under coherent, incoherent, and partially coherent conditions. For simplicity, specific coherence values were assigned, though they are typically related to spatial distances. To analyze further, we calculated scattering contrast and illumination uniformity under various illumination and coherence conditions.

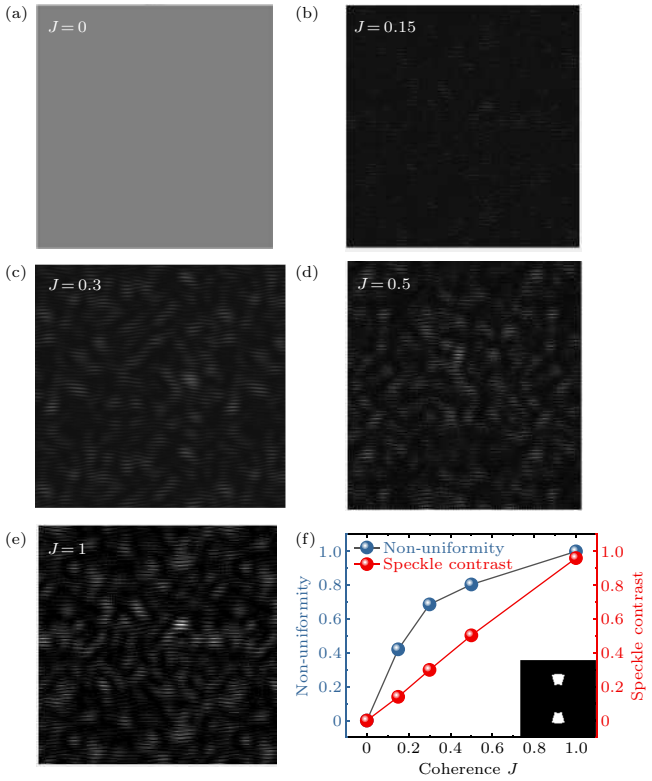


Fig. 7. Speckle effect on the uniformity and contrast of the mask plane field (dipole mode).

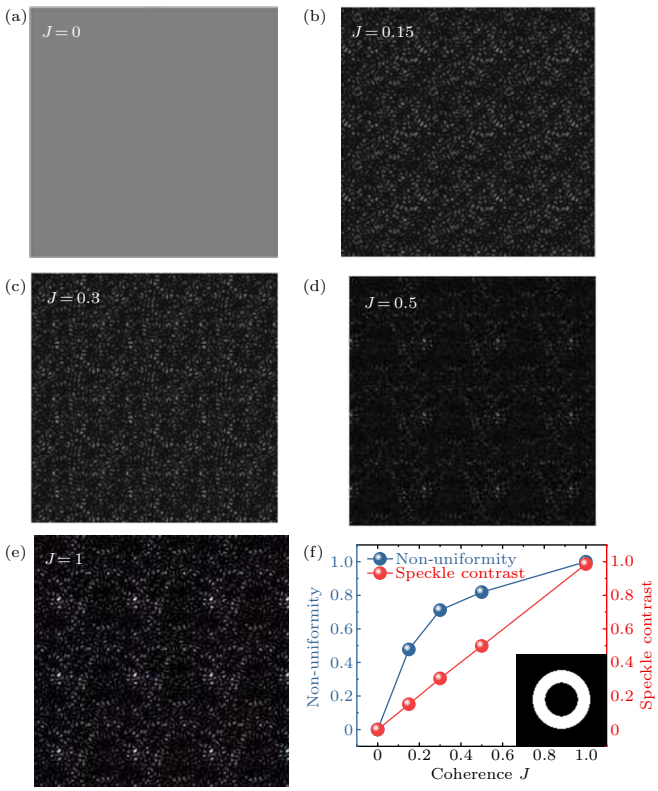


Fig. 8. Speckle effect on the uniformity and contrast of the mask plane field (annular mode).

To better illustrate the impact of coherence on the mask field uniformity and speckle contrast, the results are shown as point-line diagrams in Figs. 7 and 8. These figures show that as the coherence increases, the speckle contrast increases nearly linearly, approaching the coherence level, while the mask field non-uniformity also rises. For example, with annular illumination, increasing the coherence from 15% to 30% raises non-uniformity from 47.73% to 71.16%, and the speckle contrast from 15.11% to 30.49%. This indicates a direct relationship between the prominence of speckle effects and the coherence.

The standard requirement for two-pole annular illumination is typically over 97% uniformity. This study uses 97% as a benchmark to calculate the coherence levels for different modes that meet this criterion, analyzing the coherence required to achieve 97% uniformity under various conditions, as shown in Fig. 9.

The results indicate that as the coherence increases, illumination uniformity decreases (illumination non-uniformity increases). To meet the requirement of illumination uniformity greater than 97%, the coherence for two-pole illumination must be less than 0.72%, and for annular illumination, it must be lower than 0.5%. At this point, the corresponding speckle contrasts are 0.76% and 0.5%.

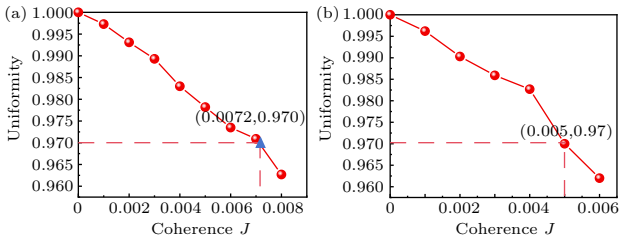


Fig. 9. The effect of different coherence levels on illumination uniformity: (a) dipole illumination, and (b) annular illumination. The maximum coherence that achieves illumination uniformity greater than 97% is calculated for each. The coherence factors for both types of illumination are $\sigma = [0.4, 0.7]$.

3.3. Coherent and partially coherent imaging

In the previous section, the influence of the spatial coherence of the light field on the scattering effect was analyzed in detail. In order to further investigate the changes in the imaging effect under different spatial coherence, light fields with different spatial coherence were selected, and field-of-view imaging was carried out by annular illumination as an example. The results are shown in Fig. 10.

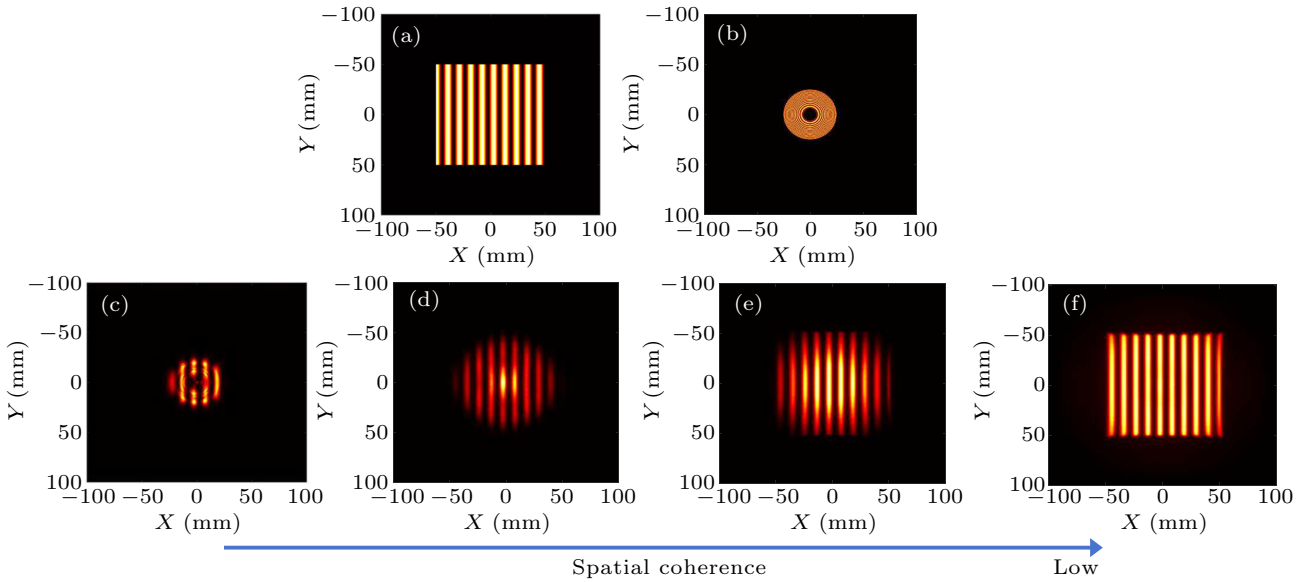


Fig. 10. The effect of coherence on field-of-view imaging. (a) Field-of-view pattern. (b) Ring-illuminated optical pupil. (c)–(f) Field-of-view imaging with coherence from high to low.

Examining the results of the figure above, it is obvious that the spatial coherence of the light field has a significant effect on the field-of-view imaging. As the spatial coherence decreases, the imaging pattern gradually tends to be consistent with the original field-of-view pattern. This indicates that the interference effect in the imaging process is weakened under low coherence conditions, resulting in less distortion of the image and a more uniform distribution of the light intensity. The high coherence makes the interference phenomenon more prominent, leading to a strong scattering effect and light intensity undulation during the imaging process; the energy distribution shows a large inhomogeneity, which in turn affects the imaging accuracy and the reproduction of pattern details. Reducing the coherence helps to mitigate these interferences and allows the imaging system to better reproduce the details in the field-of-view. Specific pattern-related analysis metrics will be discussed in detail in the next subsection, which further reveals the mechanism of the spatial coherence's impact on the imaging quality by quantitatively analyzing key parameters such as line edge roughness (LER) and line width roughness (LWR).

In optical imaging, LER is a critical parameter used to measure the irregularities of edge lines in an image,[33] particularly in photolithography. LER describes the local fluctuations of a line's edge, which arise from irregularities caused by the optical system, mask defects, process variations and other factors during the imaging process. LER can be measured using a high-resolution critical dimension scanning electron microscope (CD-SEM).[34] To obtain the LER, the local positions of the line edge must first be measured at regular intervals (denoted as Δ). LER is a measure of the irregularity of edge lines, typically used to describe the extent to which the edge deviates from the ideal straight line in space. It is usually represented by calculating the root mean square (RMS) of the deviations of edge points from the ideal line.[35]

The second section introduced the imaging principles of coherent, incoherent and partially coherent light. To study the effects of coherence on imaging, we analyzed object imaging at different coherence levels and calculated the LER, with the results shown in Figs. 11 and 13.

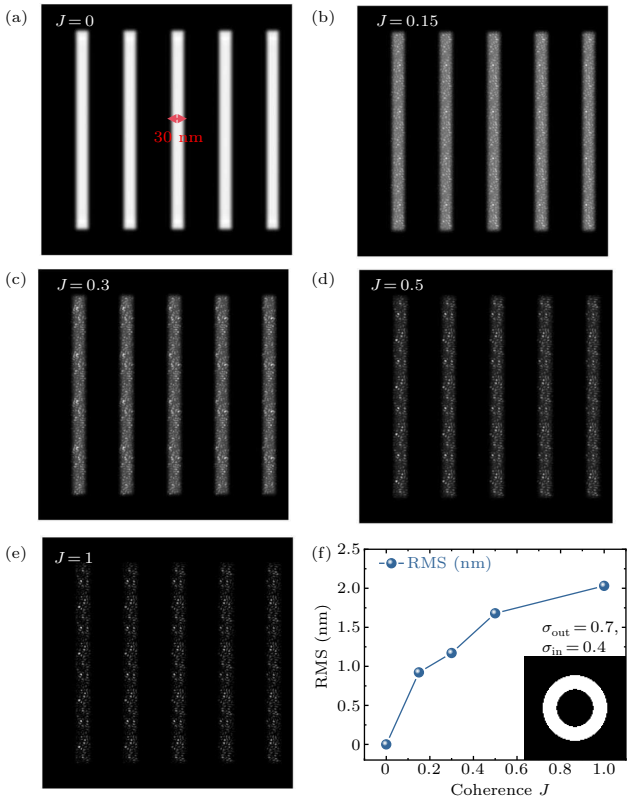


Fig. 11. Imaging of mask and RMS under different coherences (annular mode, $\sigma_{\text{out}} = 0.7$, $\sigma_{\text{in}} = 0.4$).

Coherence has a significant impact on the LER. Changes in coherence directly affect imaging quality and the sharpness of line edges. From the above figure, it can be observed that as the coherence increases, the clarity of the spatial image patterns decreases, and the corresponding LER decreases. Partially coherent light typically has a broader spectrum and greater spatial spread, which allows the light to 'average out' some of the minor irregularities introduced by the system or materials during imaging. This results in smoother edges and lower LER. In contrast, fully coherent light has stable phase relationships, making it more effective at revealing all the subtle irregularities caused by the system or materials. Therefore, when imaging with fully coherent light, even the smallest defects on the surface or mask are precisely captured in the final image, leading to rougher edges and higher LER. The greater the coherence, the greater the LER. This means that imaging with high-coherence light results in more pronounced roughness along the edges, whereas using partially coherent light helps to reduce this roughness, resulting in smoother edges.

The peak signal-to-noise ratio (PSNR) is a commonly used metric for evaluating image quality, measuring the ratio between image signal and noise. It is typically used to assess the performance of compression, denoising, or other image processing algorithms, reflecting the similarity between the processed image and the original image. The structural similarity index (SSIM) on the other hand, is a perceptual-driven metric for image quality evaluation, focusing on assessing the similarity of images in terms of brightness, contrast and structure. Unlike the PSNR, the SSIM aligns more closely with human visual perception of image quality.

We calculated the PSNR and SSIM for the imaging results above, as shown in Fig. 12. The results indicate that when the coherence is 0, the PSNR values exceed 30 dB, suggesting good image quality, while the SSIM values are close to 1. As the coherence increases, both metrics decrease and the images also reveal that the imaging quality becomes progressively blurrier.

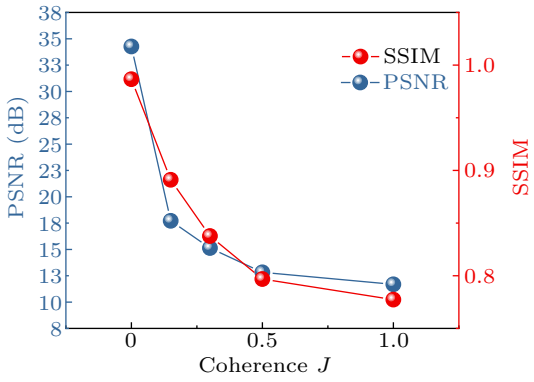


Fig. 12. PSNR and SSIM of imaging patterns under different coherences (annular mode, $\sigma_{\text{out}} = 0.7, \sigma_{\text{in}} = 0.4$).

Figures 11 and 13 reveal the impact of light source coherence on imaging under two different modes. To further analyze the effect of coherence on illumination imaging, two additional groups with different coherence factors were selected under the dipole mode as control groups. As shown in Figs. 15 and 16, the line edge RMS of their imaging was calculated, and the LER of all three imaging groups was compared, as shown in Fig. 17.

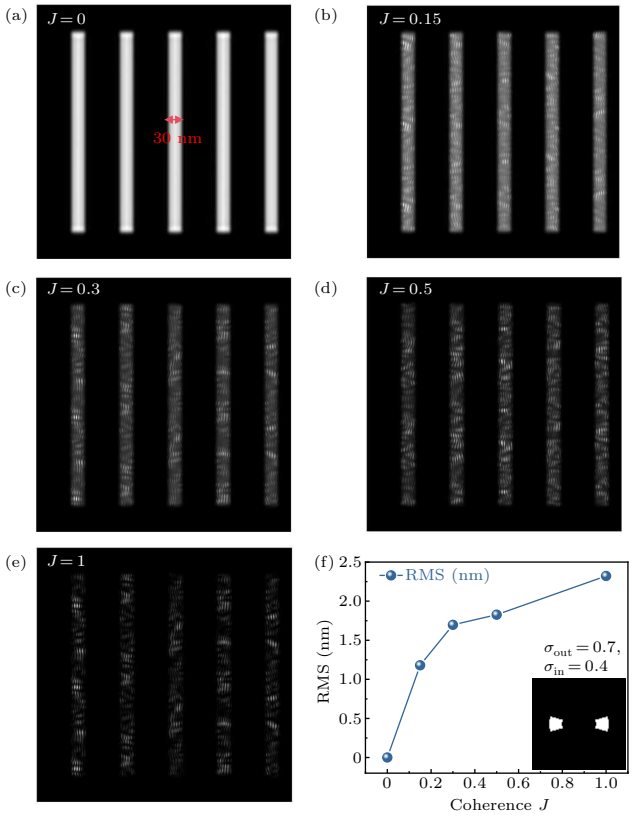


Fig. 13. Imaging of mask and RMS under different coherences (dipole mode, $\sigma_{out}=0.7, \sigma_{in}=0.4$).

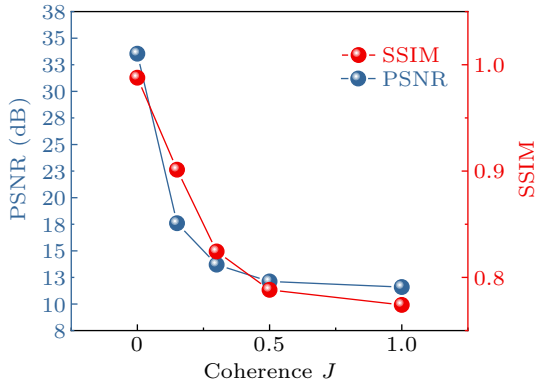


Fig. 14. PSNR and SSIM of imaging patterns under different coherences (dipole mode, $\sigma_{out}=0.7, \sigma_{in}=0.4$).

From the curve in Fig. 17, it can be observed that when the coherence level is the same, the larger the ring width, the smaller the RMS value, resulting in lower LER and better imaging quality. As the coherence increases, in addition to the previously observed increase in the LER, the larger the ring width, the slower the increase in the RMS value. This indicates that it is less affected by spatial coherence, leading to slightly better imaging quality. From the SSIM and PSNR curves in Fig. 18, it can be observed that as the ring width increases, under the same coherence level, both the SSIM and PSNR values become larger, indicating better image quality.

The above results indicate that under the same illumination mode, different partial coherence factors lead to different imaging outcomes. Compared to the other two groups, the point light source distribution in group $\sigma=[0.2,0.7]$ is

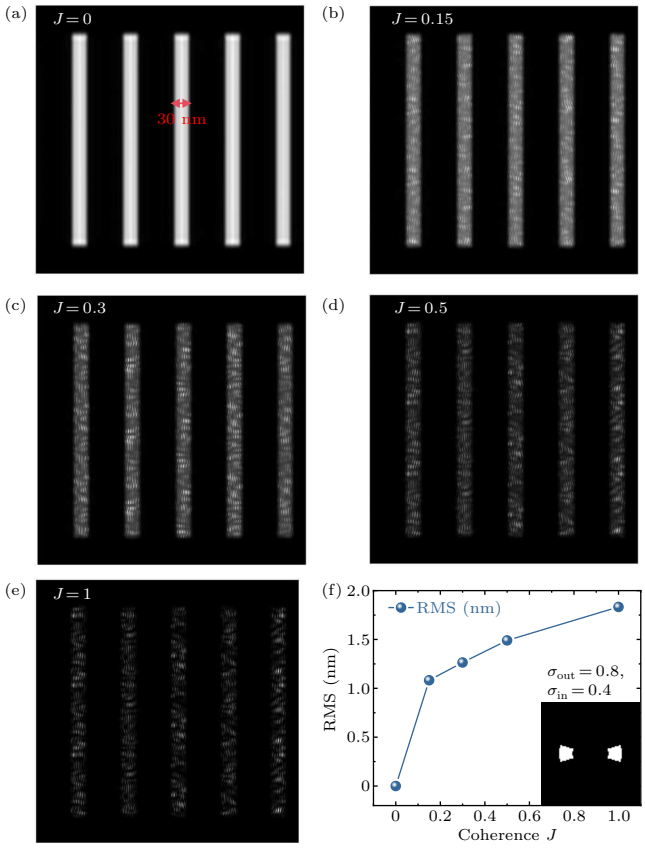


Fig. 15. Imaging of mask and LER under different coherences (dipole mode, $\sigma_{out}=0.8, \sigma_{in}=0.4$).

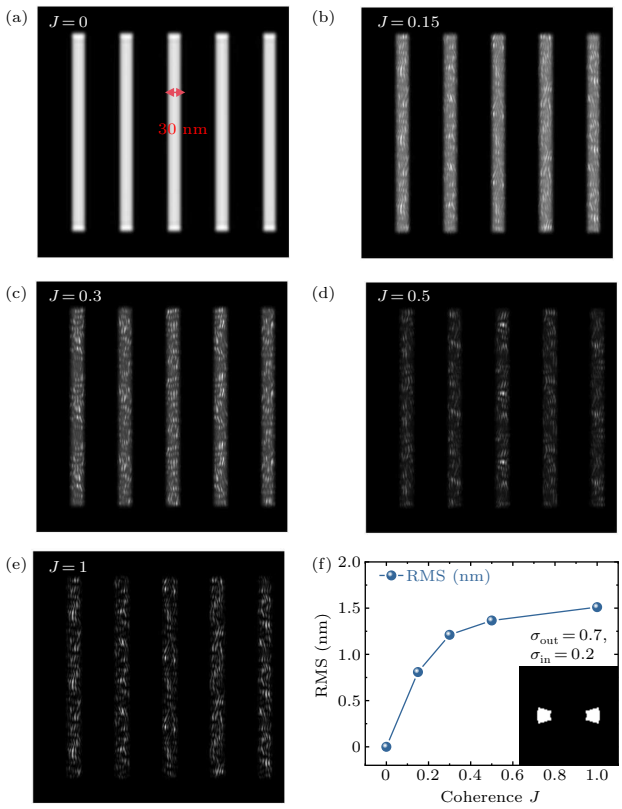


Fig. 16. Imaging of mask and LER under different coherences (dipole mode, $\sigma_{out}=0.7, \sigma_{in}=0.2$).

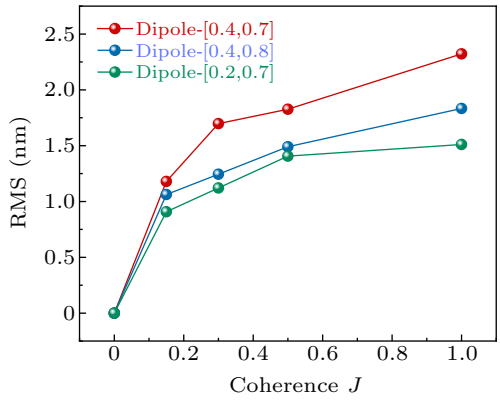


Fig. 17. The impact of the partial coherence factor on the LER in dipole mode imaging. The roughness is represented by the RMS value of the line edge.

more dispersed. Under the same spatial coherence distribution, the average spatial coherence for $\sigma = [0.2, 0.7]$ is lower than that of $\sigma = [0.4, 0.7]$ and $\sigma = [0.4, 0.8]$ because the average distance between points is greater. Therefore, it is less affected by spatial coherence, resulting in better imaging quality.

LWR refers to the irregularities and fluctuations at the edges of lines formed during etching or lithography in the semiconductor manufacturing process. It is an important parameter for measuring process precision and product quality. To further investigate the imaging quality, the imaging and LWR at different line widths on the mask were calculated separately, as shown in Fig. 20.

As can be seen from the figure, LWR is related to the line width on the object plane and the coherence of the light source. As the coherence increases, the LWR of the imaging pattern also increases, with smaller sizes being more sensitive to changes in coherence. Among the imaging results at different line widths, the larger the line width, the smaller the LWR. Both the 30 nm and 20 nm line widths can achieve relatively clear images with low LWR when the coherence is below 0.15. However, the 10 nm line width, due to its smaller size, is more susceptible to coherence effects, resulting in edge distortion and the highest LWR among the three. The SSIM and PSNR curves in Fig. 21 also support this conclusion.

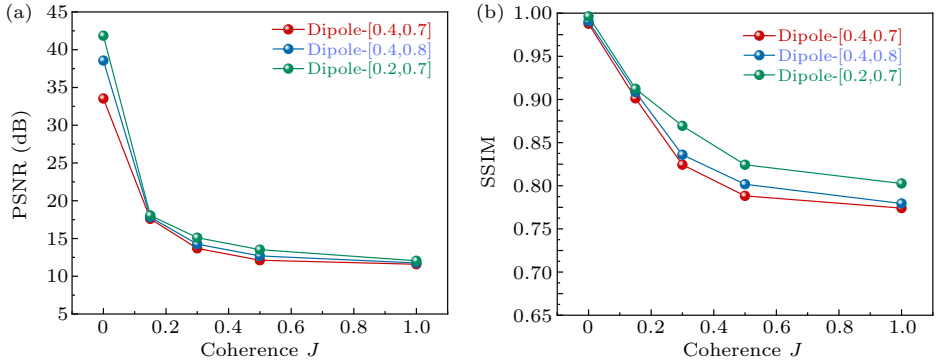


Fig. 18. The impact of the partial coherence factor on the (a) PSNR and (b) SSIM in dipole mode imaging.

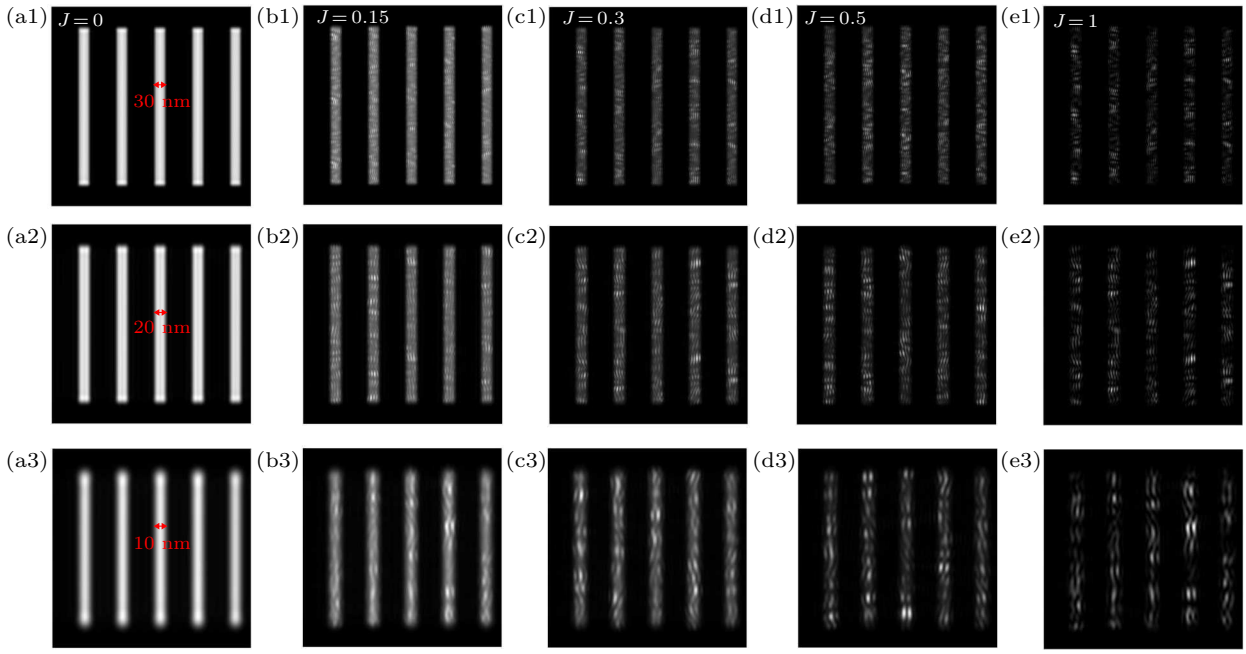


Fig. 19. Spatial images of different line widths under varying coherence levels. The three rows from top to bottom represent imaging results for line widths of 30 nm, 20 nm, and 10 nm under different coherence conditions, respectively. Panels (a)–(e) represent the imaging of three line widths at coherences of 0, 0.15, 0.3, 0.5, and 1, respectively.

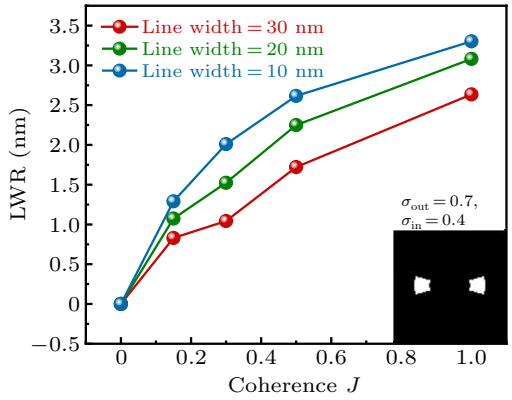


Fig. 20. The impact on LWR under different line widths. The curve represents the LWR of the imaging results. Red, blue and green respectively represent the roughness results for line widths of 30 nm, 20 nm, and 10 nm.

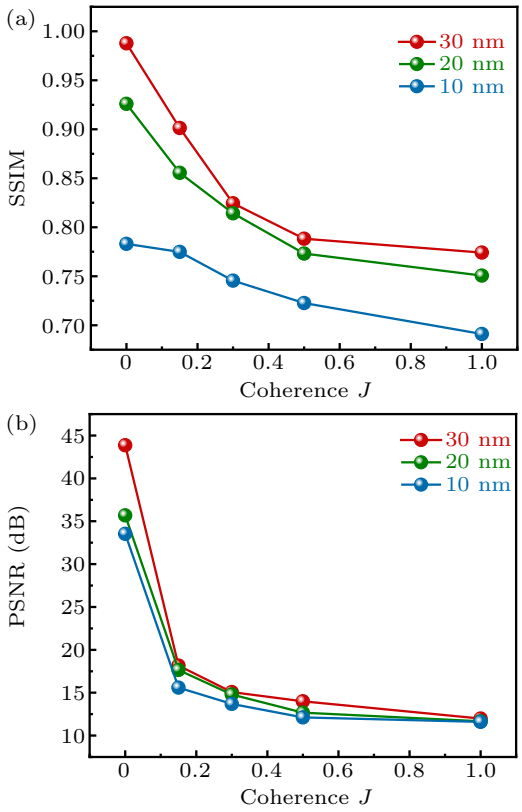


Fig. 21. The impact on (a) SSIM and (b) PSNR under different linewidths.

4. Conclusion

FELs with high temporal and spatial coherence can impact the uniformity of the illumination field and cause speckle effects, therefore reducing image quality. Traditional models often assume the light source is fully incoherent, neglecting the effects of partial coherence on imaging. To address this, this paper introduces a simulation method using random phase and a model based on the mutual intensity propagation theory to study imaging in the illumination field. The method divides the beam into temporal and spatial coherence cells and analyzes how temporal coherence affects spatial coherence. Simulations are conducted to evaluate partially coherent imaging at different spatial coherence levels, calculating LER, LWR, PSNR and SSIM. Additionally, the LWR for various object-side line widths is examined. The study also looks at speckle patterns caused by spatial coherence with different pupil shapes and their effects on speckle contrast. The results show that the speckle contrast increases with spatial coherence. As temporal coherence cells increase, the speckle effect diminishes. For uniform illumination, the spatial coherence for two-pole and annular illumination should be below 0.72% and 0.5%, with corresponding speckle contrast values of 0.76% and 0.5%. As the spatial coherence rises, the LER and LWR decrease, improving the imaging quality. When the coherence is 0, the PSNR values exceed 30 dB, suggesting good image quality, and the SSIM values are close to 1. As the coherence increases, both metrics decrease, and it can also be observed from the images that the imaging quality becomes progressively blurrier. The study finds that the pupil's partial coherence factor also affects the image quality, i.e., wider ring widths yield better results. As the ring width increases, under the same coherence level, both the SSIM and PSNR values become larger, indicating a better image quality. At all three line widths, increasing coherence results in a higher LWR in the imaging patterns, with smaller line widths being more significantly affected. Both the 30 nm and 20 nm line widths can achieve relatively clear images with low LWR when the coherence remains below 0.15. However, due to its smaller size, the 10 nm line width is more sensitive to coherence effects, leading to edge distortion and the highest LWR among the three. Achieving higher precision imaging at such small line widths will require further research and exploration in the future.

Acknowledgment

Project supported by Zhangjiang Laboratory.

References

[1] Kwan T, Dawson J M and Lin A T 1977 *The Free Electron Laser* (Springer) pp. 486–506
[2] Kim K J, Huang Z and Lindberg R 2017 *Synchrotron Radiation and Free-Electron Lasers* (Cambridge: Cambridge University Press) pp. 23–25
[3] Madey J M 1971 *J. Appl. Phys.* **42** 1906
[4] Cardman L S, Harwood L and Jefferson T 2008 *2007 IEEE Particle Accelerator Conf. (PAC)*, June 22–26, 2007, Albuquerque, United States of America, p. 58
[5] Benson S V, Beard K, Behre C, Biallas G H, Boyce J, Douglas D, Dylla F 2004 *High power lasing in the IR Upgrade FEL at Jefferson Lab Thomas Jefferson National Accelerator Facility* (*TJNAF*) (VA: USA)
[6] Kulipanov G N, Bagryanskaya E G, Chesnokov E N, Choporova Y Y, Gerasimov V V, Getmanov Y V and Vinokurov N A 2015 *IEEE Trans. on Terahertz Science and Technology* **5** 798
[7] Thompson N R, Clarke J A, Craig T, Dunning D J, Kolosov O V, Moss A and Weightman P 2015 *Proceedings of the 37th Int. Free Electron Laser Conf.*, 2015, Daejeon, Korea, p. 379
[8] Ben-Zvi I, Derbenev Y, Litvinenko V N and Merminga L 2006 *Nuclear Instruments and Methods in Physics Research Section A* **557** 28
[9] Wang G, Chao Y C, Liu C, Zhao K, Lu X, Zhuang J and Chen J 2007 *IEEE Particle Accelerator Conf.* (*PAC*), June 25–29, 2007, Albuquerque, United States of America, p. 1191

[10] Huang S L, Liu K X, Quan S W, Lin L, Zhu F and Chen J E 2011 *ii Preface* **2007** 2005

[11] Chen S, Huang S L, Li Y M, Feng L W, Zhu F, Quan S W and Chen J E 2013 *Chin. Phys. C* **37** 087001

[12] Socol Y, Kulipanov G N, Matveenko A N, Shevchenko O A and Vinokurov N A 2011 *Phys. Rev. Spec. Top. Accel. Beams* **14** 040702

[13] Socol Y, Kulipanov G N, Shevchenko O A, Vinokurov N A and Matveenko A N 2010 *13.5 nm Proc. FEL* **28** 250

[14] Goldstein M, Lee S H, Shroff Y A, Silverman P J, Williams D, Park H and Pantell R H 2005 *Proc. 2005 FEL Conf.*, August 21–26, Stanford, California, United States of America, p. 422

[15] Chen M, Chen L, Zeng A, Zhu J, Yang B and Huang H 2015 *Applied Optics* **54** 6820

[16] Voelkel R 2014 *Optical Microlithography XXVII*, March, 31, 2014, San Jose, California, United States of America, p. 530

[17] Chang C, Naulleau P, Anderson E and Attwood D 2000 *Opt. Commun.* **182** 25

[18] Anderson C N, Miyakawa R H and Naulleau P P 2011 *Extreme Ultraviolet (EUV) Lithography II*, April, 8, 2011, San Jose, California, United States of America, p. 986

[19] Naulleau P P, Anderson C N, Dean K, Denham P, Goldberg K A, Hoef B and Wallow T 2007 *Emerging Lithographic Technologies XI* March, 15, 2007, San Jose, California, United States of America, p. 265

[20] Goodman J W 2005 *Introduction to Fourier Optics* (Greenwood Village: Roberts and Company Publishers) p. 56

[21] Gbur G and Visser T D 2022 *Progress in Optics* **67** 275

[22] Young T 1802 *Phil. Trans. Roy. Soc. Lond.* **92** 387

[23] Kim Y, Seo H and Park J 2013 *Journal of Gifted/Talented Education* **23** 817

[24] Wolf E 1986 *JOSA A* **3** 76

[25] Mandel L 1995 *Optical Coherence and Quantum Optics* (Cambridge: Cambridge University Press) p. 59

[26] Zernike F 1938 *Physica* **5** 785

[27] Mandel L and Wolf E 1976 *JOSA* **66** 529

[28] Goodman J W 2007 *Speckle Phenomena in Optics: Theory and Applications* (Greenwood Village: Roberts and Company Publishers) pp. 89–113

[29] Kim S K 2021 *Micromachines* **12** 1493

[30] Stulen R H and Sweeney D W 1999 *IEEE J. Quantum Electron.* **35** 694

[31] Murakami K, Oshino T, Kondo H, Chiba H, Komatsuda H, Nomura K and Iwata H 2008 *Emerging Lithographic Technologies XII*, March, 20, 2008, San Jose, California, United States of America, p. 222

[32] Antoni M, Singer W, Schultz J, Wangler J, Escudero-Sanz I and Kruizinga B 2000 *Soft X-Ray and EUV Imaging Systems*, November, 8, 2000 San Jose, California, United States of America, p. 25–34

[33] Constantoudis V, Papavieros G, Karakolis P, Khiat A, Prodromakis T and Dimitrakis P 2019 *Materials* **12** 3972

[34] Brunner T A, Chen X, Gabor A, Higgins C, Sun L and Mack C A 2017 *Extreme Ultraviolet (EUV) Lithography VIII,* March, 24, 2017, San Jose, California, United States of America, p. 48

[35] Kim S K 2021 *Micromachines* **12** 1493